ANTIOXIDANTS & REDOX SIGNALING
Volume 9, Number 10, 2007

DOI: 10.1089/ars.2007.1720

# Forum Original Research Communication

# Continuous Wave EPR Oximetric Imaging at 300 MHz Using Radiofrequency Power Saturation Effects

YUKIHIRO HAMA,[1] KEN-ICHIRO MATSUMOTO,[1,2] RAMACHANDRAN MURUGESAN,[1,3] SANKARAN SUBRAMANIAN,[1] NALLATHAMBY DEVASAHAYAM,[1] JANUSZ W. KOSCIELNIAK,[4] FUMINORI HYODO,[1] JOHN A. COOK,[1] JAMES B. MITCHELL,[1] and MURALI C. KRISHNA[1]

## ABSTRACT

**A novel continuous wave (CW), radiofrequency (RF), electron paramagnetic resonance (EPR) oximetric imaging technique is proposed, based on the influence of oxygen concentration on the RF power saturation of the EPR resonance. A linear relationship is demonstrated between the partial oxygen pressure ($pO_2$) and the normalized signal intensity ($I_N$), defined as, $I_N = (I_{HP} - I_{LP})/I_{LP}$, where $I_{LP}$ and $I_{HP}$ refer to signal intensities at low ($P_L$) and high ($P_H$) RF power levels, respectively. A formula for the determination of $pO_2$, derived on the basis of the experimental results, reliably estimated various oxygen concentrations in a five-tube phantom. This new technique was time-efficient and also avoided the missing angle problem associated with conventional spectral-spatial CW EPR oximetric imaging. *In vivo* power saturation oximetric imaging in a tumor bearing mouse clearly depicted the hypoxic foci within the tumor.** *Antioxid. Redox Signal.* 9, 1709–1716.

## INTRODUCTION

MANY HUMAN TUMORS contain a significant fraction of hypoxic cells, because of uncontrolled cell growth and insufficient vascularization (23, 30). Tumor hypoxia is a typical pathophysiologic property that occurs across a wide variety of human malignancies. The low oxygen tension within tumors confers resistance to both radiotherapy and chemotherapy, and in many cases correlates with poor prognosis (30). Measurement of $pO_2$ in hypoxic tumors may help in better understanding of treatment resistance, and more effectively predict the outcome of therapies. Hence, there is significant interest in the development of noninvasive imaging techniques such as magnetic resonance imaging (MRI), Overhauser-enhanced MRI, positron-emission tomography (PET), and electron paramagnetic resonance imaging (EPRI), to evaluate the oxygenation status and heterogeneity of hypoxia in tumors (6, 13, 23–25, 35). Among the various techniques, direct and quantitative measurement of oxygen is possible only by EPRI (8, 14, 15, 28).

The principle of oximetry by EPR is based on the paramagnetic nature of molecular oxygen and its interaction with the paramagnetic EPR spin probe. The effect of oxygen on the spectral properties of an exogenous spin probe can be explained by bimolecular collisions and the associated magnetic interactions

[1]Radiation Biology Branch, Center for Cancer Research, National Cancer Institute, Bethesda, Maryland.
[2]Heavy-Ion Radiobiology Research Group, Research Center for Charged Particle Therapy, National Institute of Radiological Science, Chiba, Japan.
[3]School of Chemistry, Madurai Kamaraj University, Madurai, India.
[4]Laboratory of Proteomics and Analytical Technologies, Center for Cancer Research, National Cancer Institute at Frederick, Frederick, Maryland.

that cause, via Heisenberg exchange, changes in relaxation times. Bimolecular collisions of molecular oxygen with spin probes also alter both the spin–lattice and spin–spin relaxation times. The various possible methods for observation of these collisions may be classified as $T_1$-sensitive or $T_2$-sensitive and are treated in detail by Hyde and Subczynski (10). Therefore, the effects of $O_2$ on EPR spectra can be distinguished as $T_1$ and $T_2$ effects. Correlation of EPR spectral linewidths with oxygen concentration forms the basis of EPR oximetry by $T_2$- or linewidth-sensitive methods (7, 16, 27). If narrow-line paramagnetic probes such as the trityl radicals are employed, this broadening provides a means of measuring $O_2$ concentration *in vivo* (17, 32). But the outcome of this method depends on the line shape of the EPR of the spin probe. For homogeneous lines, described by a Lorentzian line shape, it is easier to detect small changes in linewidth through changes in the signal height.

There are different approaches for $T_2$-sensitive EPR oximetry that use either the continuous wave (CW) modality (constant frequency with a field sweep) or the time-domain (termed often Fourier transform, FT) modality (33). Recently, two different approaches, called relaxo-oximetry and constant time spectral-spatial imaging are reported for *in vivo* $pO_2$ measurements (22, 26). Nevertheless, spectral-spatial imaging, by CW EPR is the widely used technique for encoding oxygen-dependent linewidth into $pO_2$ (4, 15, 18). In the spectral-spatial EPR imaging modality, projections at higher gradients require long scanning time. For example, for an image of 16 spectral projections, nearly half of the scanning time is taken up by the two highest gradient projections. Missing angle algorithms have been proposed for reducing the spectral-spatial imaging time. Nevertheless, these algorithms do not minimize the problem of long scan times. Although EPR line broadening has been useful for oximetry, the unresolved hyperfine splitting can broaden the lines of the spin probe, which may decrease the relative contribution of $O_2$ broadening to the overall linewidth.

The physical interaction of the spin probe with $O_2$ via Heisenberg exchange causes spectral broadening by decreasing $T_2$. In addition, the spin–lattice relaxation of $O_2$ is so short that every collision of spin probe with $O_2$ results in a coupling to the lattice and a decrease in the effective $T_1$ of the spin probe. Relaxation times have the potential of being more sensitive than linewidths to $O_2$ concentration. $T_1$-sensitive experiments include pulsed saturation-recovery, continuous wave saturation, and rapid passage displays (11, 14). Historically, the first successful application of $T_1$-sensitive oximetry method was the development of saturation transfer (ST) EPR spectroscopy (29). ST-EPR has been used in nonconventional ways to determine spin–lattice relaxation enhancements by processes other than rotational diffusion (19, 20). Oxygen permeation profiles in lipid membranes have been computed from the $T_1$-relaxation enhancements determined by nonlinear EPR (3). Progressive saturation EPR, a well-established EPR method, has been used extensively with considerable success for spin–label localization in conjunction with site-directed spin labeling (1, 3, 31). CW ELDOR is also reported to be a simpler $T_1$-sensitive oximetric method (11). But, to our knowledge, EPRI based on CW EPR progressive saturation has not been used to obtain quantitative oxygen concentration in imaging experiments.

Here, it is demonstrated for the first time that EPR imaging using CW RF power saturation is an adequate and easy method for mapping spatial distribution of $pO_2$. This new method of oximetric imaging is simple and easy to implement, and does not require large gradients as well as long scan times.

### *Spin-lattice relaxation enhancements*

The spin-lattice relaxation time ($T_1$) can be expressed as:

$$1/T_1 = 1/T_1^0 + \Delta(1/T_1) \qquad \text{[Eq. 1]}$$

where $T_1^0$ is the intrinsic spin–lattice relaxation time and $\Delta(1/T_1)$ is the enhancement in spin–lattice relaxation rate. For Heisenberg exchange, the enhancement in spin–lattice relaxation rate, $\Delta(1/T_1)$, is given by:

$$\Delta(1/T_1) = k_{RL} \cdot [O_2] \qquad \text{[Eq. 2]}$$

Here $[O_2]$ is the oxygen concentration, and $k_{RL}$ is the rate constant for collision in the case of Heisenberg spin exchange. Since Heisenberg exchange is a contact interaction, it has been used for studying spin label localization within the phospholipids bilayers (1, 21, 31). We propose here to exploit this type of interaction at the macroscopic level to determine spatially resolved oxygen concentration by EPRI. Oxygen maps may also be obtained with variable microwave power levels, since saturation depends on oxygen concentration. The peak-to-peak amplitude of the first derivative absorption spectrum, $Y'$ can be given by,

$$Y' = K \cdot P^{1/2} \cdot (1 + P/P_{1/2})^{-1.5} \qquad \text{[Eq. 3]}$$

Here K is a proportionality constant, P is the microwave power, and $P_{1/2}$ is the microwave power required to saturate the signal to one-half of the amplitude of the spectrum where there is no saturation. The half saturation parameter in the absence ($P^\circ_{1/2}$) and presence ($P_{1/2}$) of $O_2$ can be expressed as

$$P_{1/2} = P^\circ_{1/2} + C' \cdot [O_2] \qquad \text{[Eq. 4]}$$

$C'$ is a parameter that reflects the accessibility of the spin probe to oxygen. The magnetic component of the RF field is given by:

$$B_1 = \Lambda \cdot P^{1/2} \qquad \text{[Eq. 5]}$$

Here $\Lambda$ is a constant depending on the properties of the resonator and P is incident microwave power. At very low power, the signal increases as the square root of P, whereas at high power, it decreases as 1/P.

The saturation of a homogeneously broadened conventional EPR line with increasing $B_1$ field is given by:

$$S(B_1) = S_0 \cdot B_1 / (1 + \gamma_e^2 \cdot B_1^2 \cdot T_1 \cdot T_2^{eff})^p \qquad \text{[Eq. 6]}$$

where, for a completely inhomogeneously broadened line, the exponent is $p = 1/2$ for the absorption (21) . Equation [6] with $p = 1/2$ also holds good for the integrated spectral intensity in the presence of rotational motion and of Zeeman field modulation (22). For inhomogeneously broadened EPR line, at large

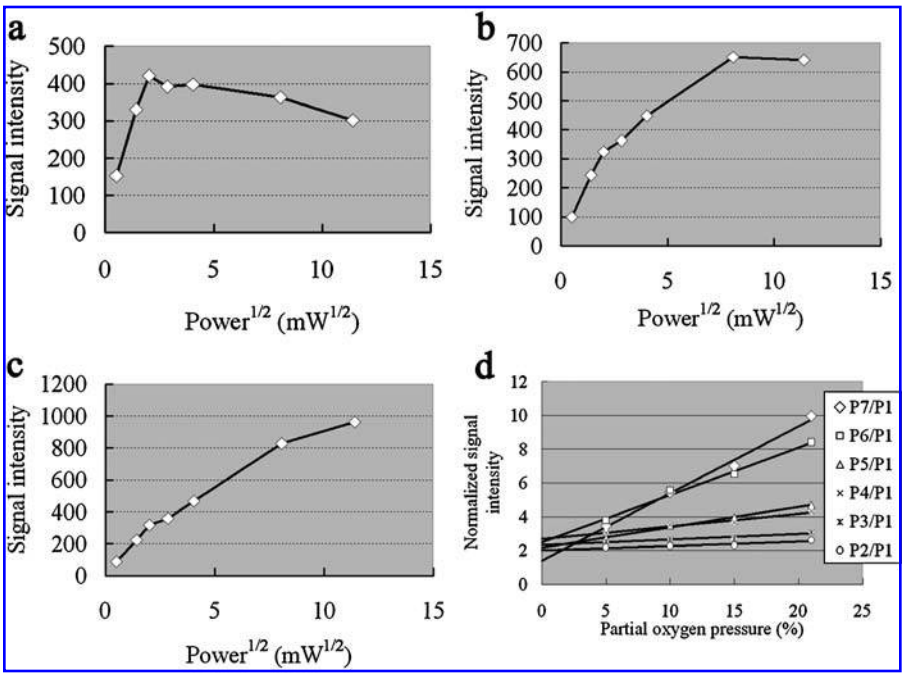


**FIG. 1. Plot showing the relationship between the radiofrequency power level and the signal intensity in various partial oxygen pressures ($pO_2$).** (**a**) $pO_2 = 0\%$; (**b**) $pO_2 = 10\%$; (**c**) $pO_2 = 21\%$. Normalized signal intensity ($I_N$) in various radiofrequency power levels was calculated and the relationship between $pO_2$ and $I_N$ was shown in (**d**): relationship between the normalized signal intensity ($I_N$) and partial oxygen pressure ($pO_2$) measured for different levels of $P_H$. Significant linear relationship was demonstrated in all radiofrequency power sets. $I_N = (I_{HP} - I_{LP})/I_{LP}$, $I_{HP}$: signal intensity at high power, $I_{LP}$: signal intensity at low power (= 0.25 mW). P1 = 0.25 mW, P2 = 4.1 mW, P3 = 8.1 mW, P4 = 16 mW, P5 = 33 mW, P6 = 65 mW, P7 = 130 mW.

B1 such that $1/\gamma B_1 < T_2 < T_1$ the susceptibility $\chi''$ may be approximated to (9):

$$\chi'' \sim 1 / \gamma B_1 T_1 \qquad \text{[Eq. 7]}$$

Thus, the intensity of the resonance mainly depends upon the $T_1$ relaxation at high $B_1$ field. The relative decrease of $T_1$ by $O_2$ can be inferred by studying the saturation of the EPR signal at high RF power. For nitroxide radicals at modest RF powers, the RF power level needed for saturation is very high. The narrow line trityl radicals can be readily saturated. In addition, the $T_1$ values of trityl radicals show only a very slight increase with increased viscosity, which is in contrast with observations on nitroxyl radicals (34). The negligible viscosity dependence of $T_1$ and strong dependence on oxygen concentration makes it an attractive probe for oximetry. To make a quantitative estimate of $pO_2$ the saturation of the resonance at two different power levels may be utilized. For this purpose, we have used the normalized signal intensity ($I_N$)

$$I_N = (I_{HP} - I_{LP}) / I_{LP} \qquad \text{[Eq. 8]}$$

as a predictive variable of $pO_2$ under various RF power levels. Here, $I_{HP}$ is the signal intensity at high power and $I_{LP}$ is the signal intensity at low power. By using the regression line calculated by $I_N$ and $pO_2$ values, power saturation oximetric imaging accurately demonstrated the $pO_2$ distribution.

## MATERIALS AND METHODS

### *Continuous wave EPR imager*

The imaging experiments were performed using a homebuilt EPR system that operates at a frequency of 300 MHz, corresponding to a resonant magnetic field of 10.8 mT (12). A Litz coil resonator (Doty Scientific, Columbia, SC) (30 mm diameter and 30 mm length) was used for EPR imaging. The experimental parameters for image acquisition were as follows; microwave power: 0.25, 4.1, 8.1, 16, 33, 65, and 130 mW, scan time: 2 s, time constant: 0.003 s, modulation amplitude: 0.18G, modulation frequency: 13.5 kHz, gradient: 1.0 G/cm.

### *Preparation of phantom*

A phantom was made with five identical tubes (inner diameter, 4.8 mm), each filled with 500 $\mu$L of 2 m*M* Oxo63, (tris[8-carboxy-2,2,6,6-tetrakis(2-hydroxymethyl)benzo[1,2-d:4,5-d′] bis(1,3)dithio-4-yl] methyl radical) solution (2, 5). Oxo63 solutions in the tubes were saturated with argon gas (0% oxygen), nitrogen–oxygen mixture containing 5%, 10%, 15% oxygen and air (21% oxygen) at room temperature for 30 min.

### *EPR image data acquisition and processing:*

A total of 18 projections were acquired with a field gradient of 1.0 G/cm, a sweep width of 4.0 G, and a field of view (FOV)

Table 1. The Slope and the Pearson's Correlation Coefficient for the Two Variables ($pO_2$ and $I_N$) for Different Radiofrequency Power Levels

| *Power levels* $P_H$ *(mW)*/$P_L$ *(mW)* | *Slope* ($S_L$) | *Pearson's correlation coefficient (r)** |
|---|---|---|
| 4.1/0.25 | 0.0257 | 0.929 |
| 8.1/0.25 | 0.0326 | 0.925 |
| 16/0.25 | 0.0755 | 0.982 |
| 33/0.25 | 0.1212 | 0.997 |
| 65/0.25 | 0.2805 | 0.995 |
| 130/0.25 | 0.3977 | 0.996 |

*Any r value of >0.9 was considered statistically significant.

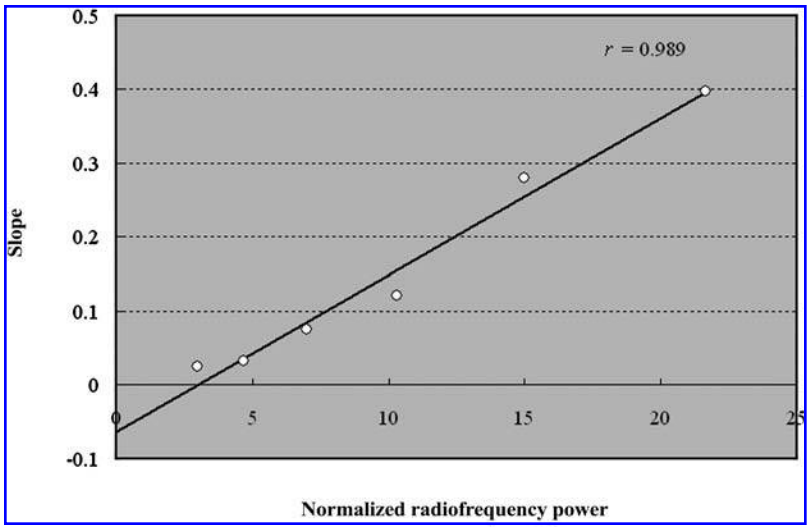


**FIG. 2. Relationship between the normalized radiofrequency power ($P_N$) and the slope of regression line ($S_L$).** The normalized radiofrequency power was calculated as: $P_N = (P_H^{1/2} - P_L^{1/2}) / P_L^{1/2}$. Significant linear relationship between $P_N$ and S is demonstrated (r = 0.989). The regression line is defined by the equation: $S_L = -0.0626 + 0.0212 \cdot P_N$.

of 40 mm × 40 mm. Image reconstruction was performed using filtered back projection algorithm on a personal computer. Two EPR imaging data sets were acquired sequentially at low and high RF powers ($P_L$ and $P_H$, respectively). Signal intensities were assessed by drawing a square-shaped region of interest (ROI) (6 × 6 pixel) in each tube, using the ImageJ software package (developed at the United States National Institutes of Health and available on the Internet at http://rsb.info.nih.gov/ij/, accessed July 1, 2007). The normalized signal intensity ($I_N$) was calculated according to the equation Eq. [8]. The regression analysis was performed using the Microsoft Excel 2003 (Microsoft, Redmond, WA). The relationship between the slope of each regression line and the normalized RF power ($P_N$) given by:

$$P_N = (P_H^{1/2} - P_L^{1/2}) / P_L^{1/2} \qquad \text{[Eq. 9]}$$

and was also derived by calculating a regression line to obtain a generalized formula for the calculation of the $pO_2$. Pearson's product moment correlation coefficients (r) were computed for analysis of relationship between the $pO_2$ and $I_N$, and between $P_N$ and the slope of $pO_2$ and $I_N$. Any r value of $> 0.9$ was considered statistically significant.

## RESULTS

To verify the RF power saturation effects, line broadening was initially measured at various RF powers, P = 0.25, 4.1, 8.1, 16, 33, 65, and 130 mW (hereafter referred to as P1 to P7, respectively), using a five-tube phantom filled with 500 $\mu$L of 2 m*M* Oxo63 maintained at different oxygen concentrations as described earlier. For RF power level <4 mW, no significant saturation-induced broadening was observed. Therefore, power levels >4 mW were used for high power measurements for oximetric imaging. However, the low power ($P_L$) was chosen to be fixed at 0.25 mW throughout the study because 0.25 mW was the maximally available level of the power where there is no saturation. Normalized EPR signal intensities of Oxo63 for

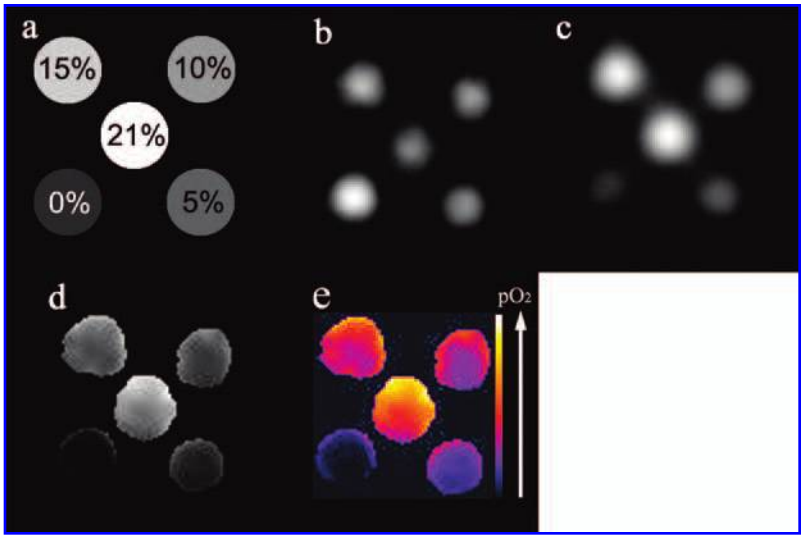


**FIG. 3. Two-dimensional oximetric imaging of a five-tube phantom.** (**a**) Spatial arrangement and characteristics of the phantom consisting of five cylindrical tubes of 4.8 mm internal diameter, each containing 2 m*M* aqueous solution of Oxo63 saturated with at different $pO_2$ levels (indicated in percent). (**b**) Signal intensity map obtained by low radiofrequency power (0.25 mW). (**c**) Signal intensity map obtained by high radiofrequency power (130 mW). (**d**) Oxygen map calculated from the two images **b** and **c.** (**e**) Color-coded oximetric image. *Color bar* indicates the $pO_2$ levels.

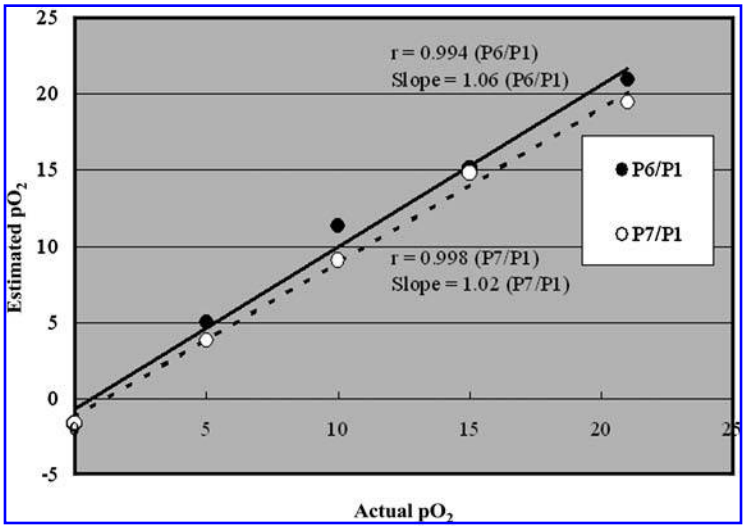


**FIG. 4. Plot illustrating the accuracy the power saturation method to estimate the $pO_2$.** r = 0.994 and slope = 1.06 for P6/P1, r = 0.998 and slope = 1.02 for P7/P1.

various oxygen concentrations were computed and relationship between $pO_2$ and $I_N$ was obtained for various $P_H$ values (Fig. 1). A significant linear relationship between $pO_2$ and $I_N$ was observed for all different power levels. The statistical parameters, the Pearson's correlation coefficient (r) and the slope of each regression line ($S_L$), are collected in Table 1. The strong correlation, observed for $P_H > 33$ mW, suggests that for better accuracy of oximetric imaging by this technique, the $P_H$ needs to be at least as high as 33 mW. The slope of each regression line increased progressively with the magnitude of power used for saturation, suggesting that the sensitivity of the method depends upon the high power level ($P_H$) used in the experiment. The intercept ($I_N$ at $pO_2 = 0$), computed from these various experiments, was found to be 2.17 ± 0.45 (mean ± standard deviation) following the relation,

$$I_N = 2.17 + S_L \cdot pO_2 \qquad \text{[Eq. 10]}$$

Using the values of the slope (Table 1), relationship between the normalized power ($P_N$) and the slope ($S_L$) was obtained by the data given in Table 1.

$$S_L = -0.0626 + 0.0212 \cdot P_N \qquad \text{[Eq. 11]}$$

Significant linear relationship (Fig. 2) between the two variables ($P_N$ and $S_L$) was observed (r = 0.989). Using Eq. [10] and Eq. [11], the spatial distribution of oxygen concentration was computed from intensity images acquired at two different power levels. Two-dimensional oximetric images obtained by using low (P1) and high (P7) RF power are presented in Fig. 3. Differences in $pO_2$ among the five tubes can be readily recognized (Figs. 3d and e). We have also computed the $pO_2$ of each tube using Eq. [10] and Eq. [11] and compared them with the expected values in Fig. 4. For high power levels $P_H$, P7 (130 mW) and P6 (65 mW) were selected, because better correlation and higher $S_L$ values were observed (Fig. 1). The linear relationship between the given $pO_2$ and the estimated $pO_2$ from the oximetric images is significant for both the power levels (r = 0.998 for P7/P1, r = 0.994 for P6/P1), validating the viability of this technique. For a comparative evaluation of the performance of the power saturation method, oximetric imaging of a phantom was performed by projection reconstruction spectral-spatial imaging (PRSSI) using the same EPR imager and the results are presented in Fig. 5. The image acquisition parameters are given in Table 2. The quality and the resolution of power saturation image were feasible in a phantom study with substantially shorter acquisition time compared to the PRSSI. To examine the feasibility of the power saturation imaging approach *in vivo*, a tumor bearing mouse was imaged at two power levels (P1 and P7). The resultant power saturation image encoding the $pO_2$ demonstrated a semiquantitative discrimination

TABLE 2. COMPARISON OF IMAGE ACQUISITION PARAMETERS

| *Imaging methods (figure number)* | *Number of projections* | *Time required* | *Maximum gradient (G/cm)* |
|---|---|---|---|
| Power saturation image (Fig. 5b) | 18 × 2 = 36 | 10 min 12 s (17 s × 36 = 612 s) | 0.5 |
| PRSSI (Fig. 5c) | 19 × 18 = 342 | 1 h 36 min 54 s (17 s × 342 = 5814 s) | 4 |

Sweep time, number of points, modulation amplitude, time constant, field of view, and number of averaging are same between the two image acquisition methods: sweep time = 17 s (including 1 s for reversing the magnetic field), number of points = 1024, modulation frequency = 13.5 kHz, modulation amplitude = 0.18 G, time constant = 0.1 s, field of view = 40 × 40 mm, number of averaging = 1. PRSSI: projection reconstruction spectral-spatial imaging.

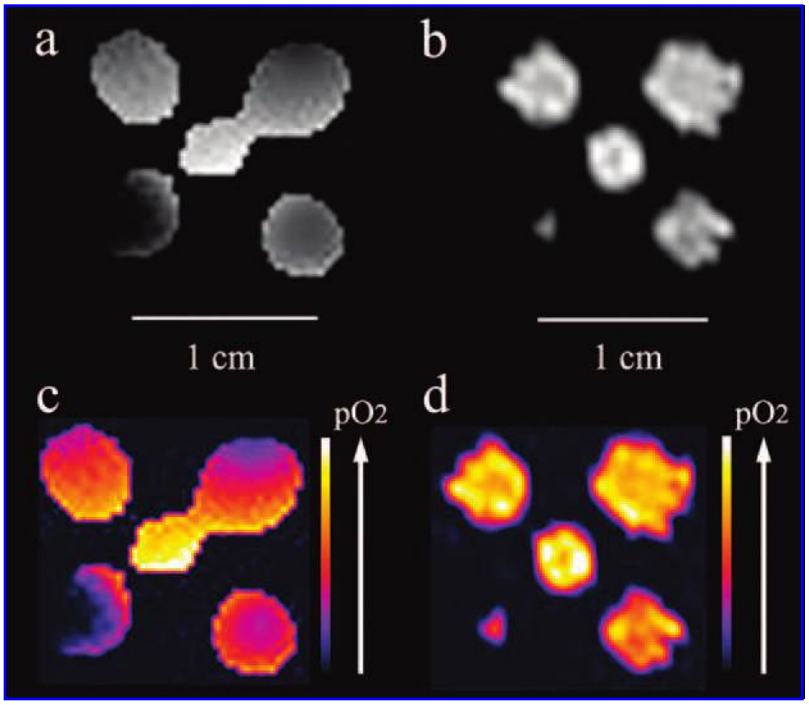


**FIG. 5. Oximetric imaging of a five tube phantom performed by projection reconstruction spectral-spatial imaging and power saturation method.** Spatial arrangement and characteristics of the phantom containing 2 m*M* Oxo63 aqueous solution with different $pO_2$ levels are the same as that used in Fig. 3. (**a**) Power saturation image obtained by two different radiofrequency power levels (0.25 and 130 mW). (**b**) Projection reconstruction spectral-spatial image. (**c**) and (**d**) Color-coded oximetric images of **a** and **b,** respectively. *Color bar* indicates the $pO_2$ levels in each image.

between normoxic (left, normal leg) and hypoxic (right, tumor) (Fig. 6). The image acquisition parameters were the same as those used in the phantom study.

## DISCUSSION

As indicated earlier, the spectral-spatial imaging by CW EPR is the widely used technique for encoding oxygen-dependent linewidth into $pO_2$. Results of this study demonstrate that the saturation effects, evoked by high RF power, and the eventual signal intensity changes might be applicable to noninvasive and quantitative assessment of oxygen concentration. The results presented in Fig. 5, show that while the PRSSI gives a near distortion-free image, the discriminating performance of the power saturation technique was comparable or superior. The spectral-spatial imaging uses linewidth of paramagnetic spin probes because it is proportional to $pO_2$ unless there is no power saturation. To obtain a 2D oximetric image, data for a 3D image (2D spatial and 1D spectral) is to be acquired (22). In contrast, the power saturation method directly maps 2D oxygen concentration from just two (one low power and one high power) 2D spatial images. Fair comparison between the PRSSI and the power saturation imaging is impossible due to the substantial differences in image acquisition method, but the short acquisition time with acceptable quality in power saturation imaging indicates the power saturation imaging method is feasible for oximetric imaging.

We envisage yet another advantage for the power saturation technique. The dynamic range of $I_N$ values is relatively high. For example, for $P_H$ of 130 mW, the dynamic range in $I_N$ is

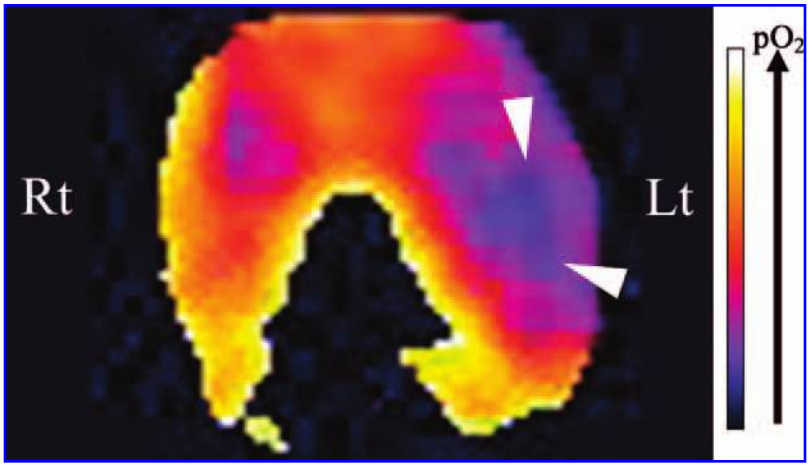


**FIG. 6. *In vivo* power saturation oximetric image of the tumor-bearing mouse.** Power saturation image obtained by two different radiofrequency power levels (0.25 and 130 mW) clearly depicts the hypoxic foci of the tumor (squamous cell carcinoma) (*arrowheads*) in the left leg (Lt). Rt: normal leg; Lt: tumor-bearing leg. A female C3H mouse with SCC tumor on the right hind leg was anesthetized by 1.5% isoflurane in medical air flow (700 mL/min). Oxo63 was administrated by a bolus i.v. injection (0.75 μmol/g b.w./min) followed by a continuous i.v. infusion (0.06 $\mu$mol/g b.w./min). The image data acquisition was as described in the text.

0.853 (log [9.956/1.397]). For the linewidth based PRSSI, dynamic range in the linewidth variation is 0.165 (log [0.259/0.177]), because the linewidth changes from 0.177 G at 0% $pO_2$ to 0.259 G at 21% $pO_2$. For the conventional spatial EPR image (Fig. 3b), dynamic range in the signal intensity is 0.226 (log [214.6/127.7]), because the signal intensities of 0% $pO_2$ and 21% $pO_2$ are 214.6 and 127.7 in arbitrary unit (a.u.), respectively. The superior dynamic range in $I_N$ may be useful when hypoxic and normoxic cores are present in an object to be imaged simultaneously. One may expect the high RF power used in this technique to pose some problems when this technique is extended to quantitative *in vivo* oximetric imaging studies. But our initial investigations show that even for a high power of 130 mW, there was no increase in the rectal temperature of mouse (data not shown). In spatial EPR imaging an intensity map represents the free radial distribution but it is blurred depending on the spectrum lineshape of the spin probe. Since the lineshape as well as the linewidth will change due to the power saturation effect, convolution and deconvolution approach cannot be applied in the current power saturation imaging technique. To establish the quantitative *in vivo* power saturation oximetric imaging, further investigations which eliminate the confounding factors (*e.g*., image blurring, dose optimization of the spin probe) are necessary. The current *in vivo* oximetric image was not given quantitatively, however, the high dynamic range, the short data acquisition time and no significant heating effects may allow us to further investigate the quantitative *in vivo* oximetric imaging using the power saturation technique.

In conclusion, this preliminary study demonstrates that CW EPR power saturation technique is feasible for oximetric imaging as a rapid and highly discriminating method.

## ACKNOWLEDGMENTS

This research was supported by the Intramural Research Program of the NIH, National Cancer Institute, Center for Cancer Research. Dr. Hama is thankful to the Japan-U.S. Radiological Exchange Association and the National Defense Medical College, Japan for partial finance support.

## ABBREVIATIONS

CW, continuous wave; EPRI, electron paramagnetic resonance imaging; MRI, magnetic resonance imaging; PRSSI, projection reconstruction spectral-spatial imaging; ST, saturation transfer.

## REFERENCES

1. Altenbach C, Greenhalgh DA, Khorana HG, and Hubbell WL. A collision gradient method to determine the immersion depth of nitroxides in lipid bilayers: application to spin-labeled mutants of bacteriorhodopsin. *Proc Natl Acad Sci USA* 91: 1667–1671, 1994.
2. Ardenkjaer–Larsen JH, Laursen I, Leunbach I, Ehnholm G, Wistrand L G, Petersson JS, and Golman K. EPR and DNP properties of certain novel single electron contrast agents intended for oximetric imaging. *J Magn Reson* 133: 1–12, 1998.
3. Dzikovski BG, Livshits VA, and Marsh D. Oxygen permeation profile in lipid membranes: comparison with transmembrane polarity profile. *Biophys J* 85: 1005–1012, 2003.
4. Elas M, Williams BB, Parasca A, Mailer C, Pelizzari CA, Lewis MA, River JN, Karczmar GS, Barth ED, and Halpern HJ. Quantitative tumor oxymetric images from 4D electron paramagnetic resonance imaging (EPRI): methodology and comparison with blood oxygen level-dependent (BOLD) MRI. *Magn Reson Med* 49: 682–691, 2003.
5. Golman K, Petersson JS, Ardenkjaer–Larsen JH, Leunbach I, Wistrand LG, Ehnholm G, and Liu K. Dynamic *in vivo* oxymetry using overhauser enhanced MR imaging. *J Magn Reson Imaging* 12: 929–938, 2000.
6. Grucker D. Oximetry by magnetic resonance: applications to animal biology and medicine. *Prog Nucl Mag Res Sp* 36: 241–270, 2000.
7. Halpern HJ, Yu C, Peric M, Barth E, Grdina DJ, and Teicher BA. Oxymetry deep in tissues with low-frequency electron paramagnetic resonance. *Proc Natl Acad Sci USA* 91: 13047–13051, 1994.
8. Halpern HJ, Yu C, Peric M, Barth ED, Karczmar GS, River JN, Grdina DJ, and Teicher BA. Measurement of differences in $pO_2$ in response to perfluorocarbon/carbogen in FSa and NFSa murine fibrosarcomas with low-frequency electron paramagnetic resonance oximetry. *Radiat Res* 145: 610–618, 1996.
9. Hyde JS. Saturation of the magnetic resonance absorption in dilute inhomogeneously broadened systems. *Phys Rev* 119: 1492–1495, 1960.
10. Hyde JS,and Subczynski WK. Spin-label oximetry. In: *Biological Magnetic Resonance 8, Spin Labeling Theory and Applications*, Berlinear LJ and Reuben J, eds. New York: Plenum, 1989, pp. 399–425.
11. Hyde JS, Ym JJ, Feix JB, and Hubbell WL. Advances in spin label oximetry. *Pure Appl Chem* 62: 255–260, 1990.
12. Koscielniak J, Devasahayam N, Moni MS, Kuppusamy P, Yamada K, Mitchell JB, Krishna MC, and Subramanian S. 300 MHz continuous wave electron paramagnetic resonance spectrometer for small animal *in vivo* imaging. *Rev Sci Instrum* 71: 4273–4281, 2000.
13. Krishna MC, English S, Yamada K, Yoo J, Murugesan R, Devasahayam N, Cook JA, Golman K, Ardenkjaer–Larsen JH, Subramanian S, and Mitchell JB. Overhauser enhanced magnetic resonance imaging for tumor oximetry: coregistration of tumor anatomy and tissue oxygen concentration. *Proc Natl Acad Sci USA* 99: 2216–2221, 2002.
14. Kuppusamy P. EPR spectroscopy in biology and medicine. *Antioxid Redox Signal* 6: 583–585, 2004.
15. Kuppusamy P, Afeworki M, Shankar RA, Coffin D, Krishna MC, Hahn SM, Mitchell JB, and Zweier JL. *In vivo* electron paramagnetic resonance imaging of tumor heterogeneity and oxygenation in a murine model. *Cancer Res* 58: 1562–1568, 1998.
16. Kuppusamy P, Shankar RA, and Zweier JL. *In vivo* measurement of arterial and venous oxygenation in the rat using 3D spectral-spatial electron paramagnetic resonance imaging. *Phys Med Biol* 43: 1837–1844, 1998.
17. Mailer C, Robinson BH, Williams BB, and Halpern HJ. Spectral fitting: the extraction of crucial information from a spectrum and a spectral image. *Magn Reson Med* 49: 1175–1180, 2003.
18. Maltempo MM, Eaton SS, and Eaton GR. Spectral-spatial two dimensional electron-paramagnetic-resonance imaging. *J Magn Reson* 72: 449–455, 1987.
19. Marsh D. Progressive saturation and saturation-transfer ESR for measuring exchange process of spin-labeled lipids and proteins in membranes. *Chem Soc Rev* 22: 329–335, 1993.
20. Marsh D and Horvath L. Influence of Heisenberg spin exchange on conventional and phase-quadrature EPR lineshapes and intensities under saturation. *J Magn Reson* 97: 13–26, 1992.
21. Marsh D and Livshits V A. Recent developments in spin labelling. *Phys Med Biol* 43: 1977–1986, 1998.
22. Matsumoto K, Chandrika B, Lohman J A, Mitchell JB, Krishna MC, and Subramanian S. Application of continuous-wave EPR spectral-spatial image reconstruction techniques for *in vivo* oxym-

etry: comparison of projection reconstruction and constant-time modalities. *Magn Reson Med* 50: 865–874, 2003.
23. Rajendran JG and Krohn KA. Imaging hypoxia and angiogenesis in tumors. *Radiol Clin North Am* 43: 169–187, 2005.
24. Serganova I, Doubrovin M, Vider J, Ponomarev V, Soghomonyan S, Beresten T, Ageyeva L, Serganov A, Cai S, Balatoni J, Blasberg R, and Gelovani J. Molecular imaging of temporal dynamics and spatial heterogeneity of hypoxia-inducible factor-1 signal transduction activity in tumors in living mice. *Cancer Res* 64: 6101–6108, 2004.
25. Subramanian S, Matsumoto K, Mitchell JB, and Krishna MC. Radio frequency continuous-wave and time-domain EPR imaging and Overhauser-enhanced magnetic resonance imaging of small animals: instrumental developments and comparison of relative merits for functional imaging. *NMR Biomed* 17: 263–294, 2004.
26. Subramanian S, Yamada K, Irie A, Murugesan R, Cook JA, Devasahayam N, Van Dam GM, Mitchell JB, and Krishna MC. Noninvasive *in vivo* oximetric imaging by radiofrequency FT EPR. *Magn Reson Med* 47: 1001–1008, 2002.
27. Swartz HM. Using EPR to measure a critical but often unmeasured component of oxidative damage: oxygen. *Antioxid Redox Signal* 6: 677–686, 2004.
28. Swartz HM and Clarkson R B. The measurement of oxygen in vivo using EPR techniques. *Phys Med Biol* 43: 1957–1975, 1998.
29. Thomas DD, Dalton LR, and Hyde JS. Rotational diffusion studies by passage saturation transfer electron-paramagnetic resonance. *J Chem Phys* 65: 3006–3024, 1976.
30. Vaupel P, Thews O, Kelleher DK, and Hoeckel M. Current status of knowledge and critical issues in tumor oxygenation. Results from 25 years research in tumor pathophysiology. *Adv Exp Med Biol* 454: 591–602, 1998.
31. Venkataraman S, Schafer FQ, and Buettner GR. Detection of lipid radicals using EPR. *Antioxid Redox Signal* 6: 631–638, 2004.
32. Williams BB, al Hallaq H, Chandramouli GV, Barth ED, Rivers JN, Lewis M, Galtsev VE, Karczmar GS, and Halpern HJ. Imaging spin probe distribution in the tumor of a living mouse with 250 MHz EPR: correlation with BOLD MRI. *Magn Reson Med* 47: 634–638, 2002.
33. Yamada K, Murugesan R, Devasahayam N, Cook JA, Mitchell JB, Subramanian S, and Krishna MC. Evaluation and comparison of pulsed and continuous wave radiofrequency electron paramagnetic resonance techniques for in vivo detection and imaging of free radicals. *J Magn Reson* 154: 287–297, 2002.
34. Yong L, Harbridge J, Quine RW, Rinard GA, Eaton SS, Eaton GR, Mailer C, Barth E, and Halpern HJ. Electron spin relaxation of triarylmethyl radicals in fluid solution. *J Magn Reson* 152: 156–161, 2001.
35. Ziemer LS, Evans SM, Kachur AV, Shuman AL, Cardi CA, Jenkins WT, Karp JS, Alavi A, Dolbier WR Jr., and Koch CJ. Noninvasive imaging of tumor hypoxia in rats using the 2-nitroimidazole 18F-EF5. *Eur J Nucl Med Mol Imaging* 30: 259–266, 2003.

Address reprint requests to:
*Murali C. Krishna*
*Building 10, Room B3-B69*
*National Institutes of Health*
*Bethesda, MD 20892-1002*

*E-mail:* murali@helix.nih.gov

Date of first submission to ARS Central, April 27, 2007; date of acceptance, May 2, 2007.

**This article has been cited by:**


1. Deepti S. Vikram, Rizwan Ahmad, Brian K. Rivera, Periannan Kuppusamy. 2008. Mapping of Oxygen Concentration in Biological Samples Using EPR Imaging. *Israel Journal of Chemistry* **48**:1, 39-43. [CrossRef]
2. Boris Epel, Subramanian V. Sundramoorthy, Colin Mailer, Howard J. Halpern. 2008. A versatile high speed 250#MHz pulse imager for biomedical applications. *Concepts in Magnetic Resonance Part B: Magnetic Resonance Engineering* **33B**:3, 163. [CrossRef]